

ImmuvIs: Hyperconvolutional Foundation Model for Imaging Mass Cytometry

Marcin Mozejko ^{*1} Dawid Uchal ^{*1} Krzysztof Gogolewski ^{*1} Piotr Kupidura ¹ Szymon Łukasik ¹
 Jakub Giezała ¹ Tomasz Nocón ¹ Kacper Pietrzyk ¹ Robert Pieniuta ¹ Mateusz Sulimowicz ¹
 Michał Orzyłowski ¹ Tomasz Siłkowski ¹ Karol Zagrodnka ¹ Eike Staub ² Ewa Szczurek ^{1,3}

Abstract

We present ImmuvIs, an **efficient convolutional foundation model** for imaging mass cytometry (IMC), a high-throughput multiplex imaging technology that handles molecular marker measurements as image channels and enables large-scale spatial tissue profiling. Unlike natural images, multiplex imaging lacks a fixed channel space, as real-world marker sets vary across studies, violating a core assumption of standard vision backbones. To address this, ImmuvIs introduces **marker-adaptive hyperconvolutions** that generate convolutional kernels from learned marker embeddings, enabling a single model to operate on arbitrary measured marker subsets without re-training. We pretrain ImmuvIs on the **largest to-date dataset**, IMC17M (28 cohorts, 24,405 images, 265 markers, over 17M patches), using self-supervised masked reconstruction. ImmuvIs outperforms SOTA baselines and ablations in virtual staining and downstream classification tasks at substantially lower compute cost than transformer-based alternatives, and is the sole model that provides **calibrated uncertainty** via a heteroscedastic likelihood objective. These results position ImmuvIs as a practical, efficient foundation model for real-world IMC modeling.

1. Introduction

Imaging Mass Cytometry (IMC) profiles protein abundances in tissues at subcellular spatial resolution by measuring metal-tagged antibodies via mass spectrometry (Giesen et al., 2014; Chang et al., 2017). IMC is increasingly central to spatially resolved single-cell analysis of healthy and dis-

¹Department of Mathematics, Informatics and Mechanics, University of Warsaw, Warsaw, Poland ²Merck Healthcare KGaA, Darmstadt, Germany ³Institute of AI for Health, Helmholtz Center Munich, Ingolstädter Landstraße 1, 85764, Neuherberg, Germany. Correspondence to: Ewa Szczurek <em.szczurek@mimuw.edu.pl>.

Preprint. February 5, 2026.

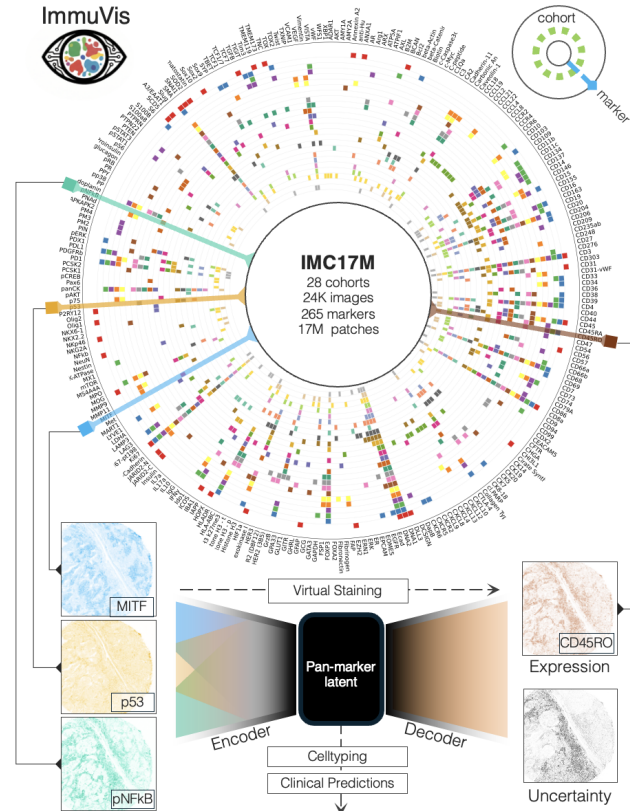


Figure 1. Motivation for ImmuvIs: real-world panel heterogeneity. IMC17M exhibits strong cohort–marker diversity (rings: cohorts; radii: markers; colored ticks: measured markers), motivating a single model that operates on arbitrary marker subsets. ImmuvIs encodes any observed panel (e.g., MITF, p53, pNFkB) into a shared pan-marker latent space for downstream phenotyping (cell typing, clinical prediction) and instantiates a task-specific decoder to virtually stain requested targets (e.g., CD45RO), outputting both expression and predictive uncertainty.

ease tissues, and both datasets and preprocessing pipelines are rapidly maturing (Milosevic, 2023; Nat. Methods Editorial, 2024). Panel richness matters: larger marker panels better resolve cell types and functional states and support mapping of tissue spatial neighborhoods (Bollhagen & Bodenmiller, 2024; de Souza et al., 2024).

Still, cohort-specific IMC panels are typically restricted to

only tens of markers because of physical channel interference that reduces the number of concurrently usable metal isotopes for antibody tagging (Bendall et al., 2012; Chevrier et al., 2018). In practice, as presented in Figure 1, cross-cohort marker overlap is limited, making **modelling and analysis across heterogeneous panels** a practical necessity (Bussi & Keren, 2024). This motivates **virtual staining**, i.e. predicting cohort-dependent *missing-marker sets* from the *measured* panel, to enable denser tissue phenotyping without additional wet-lab work (Latonen et al., 2024). Basic approaches to this task suffer from a fixed input problem, i.e. are limited to a fixed, narrow marker panel (Lo et al., 2022; Shaban et al., 2023), which prevents panel flexibility and straightforward extension to diverse marker sets. VirTues (Wenckstern et al., 2025), a recent Transformer-based model, supports variable marker inputs by concatenating marker-specific spatial tokens augmented with marker-identity encodings derived from protein language model. However, since the spatial tokens provide only a global view per marker image patch, VirTues effectively ignores crucial local marker dependencies. In contrast, variable input learning in other vision domains is often implemented via conditional operators, e.g. hypernetworks (Ha et al., 2017) and dynamic convolutions (Chen et al., 2019), that modulate the feature extractor conditioned on the input in a computationally efficient manner; yet this approach remains underused in multiplex imaging.

Virtual staining is also a **reliability problem**: when the measured marker set provides weak evidence for a target marker (e.g., rare phenotypes or atypical tissue patterns), accurate point prediction is ill-posed and visually plausible reconstructions may still be biologically wrong (Dolezal et al., 2022). In this regime, **uncertainty** must be a part of the model output, highlighting unconfident predictions. Finally, cohort-scale use places a strong emphasis on **inference time**. Transformer-heavy virtual-staining models can become increasingly slow as marker count and spatial resolution grow (Papa et al., 2024). To summarize, to the best of our knowledge, no prior virtual-staining model combines **panel flexibility** and **calibrated uncertainty** with **inference speed** for IMC.

To address these challenges, we introduce `ImmuVis`, a fully convolutional foundation model for IMC data that unifies variable-input learning, efficiency, and uncertainty in a single architecture. Our contributions are as follows:

1. **Hyperconvolutional architecture:** We introduce a channel-adaptive hyperconvolution module that provides operator-level channel adaptivity and generates convolutional kernels conditioned on learned marker embeddings, enabling a single model to process arbitrary marker combinations without architectural modification or retraining.

2. **Efficient Foundation Model:** In our primary configuration, `ImmuVis` instantiates a ConvNeXt-v2-based encoder-decoder and scales computation with spatial resolution via convolutional operators, offering substantially lower inference overhead than token-based alternatives.
3. **Uncertainty-aware learning objective:** We model predictive uncertainty via Gaussian heteroscedastic regression, producing uncertainty estimates that highly correlate with reconstruction error, making virtual staining reliability-aware rather than purely point-estimated.

We pretrain `ImmuVis` on the largest IMC dataset compiled to our knowledge (IMC17M ; 24,405 images, 265 markers, 28 datasets) using masked-channel reconstruction, and show that the learned representations transfer across datasets to state-of-the art performance in virtual staining, patch-level cell typing, and clinical prediction.

Taken together, `ImmuVis` provides a practical, panel-flexible IMC foundation model that is deployable at cohort scale and enables reliability-aware virtual staining. More broadly, it offers a general recipe for variable-input foundation models in multiplex imaging and beyond.

2. Related Work

Virtual staining under heterogeneous panels for multiplex data. Virtual staining aims at prediction of unmeasured markers, increasing phenotyping depth and enabling retrospective upgrading of legacy cohorts without additional wet-lab assays (Zidane et al., 2023; Wenckstern et al., 2025). Early approaches to this problem typically assume a fixed input panel and train U-Net-like architectures to predict new markers (Ternes et al., 2022; Shaban et al., 2023). However, these methods lack panel flexibility, as they are restricted to datasets whose panels contain markers used during training and cannot exploit additional available markers. To achieve panel flexibility, (Kraus et al., 2024) adopt a channel-extended ViT design from (Bao et al., 2024), which concatenates marker-specific spatial tokens with marker-identity encodings and processes them using a transformer model. However, this design incurs a heavy combinatorial marker×space computational cost. (Wenckstern et al., 2025) mitigated this limitation via marker–space attention factorization and the use of pretrained language model embeddings as marker encodings enabling predictions for previously unseen markers. Still, in these transformer tokenization-based designs, marker identity is injected *after* tokenization and therefore may underutilize fine-grained, local cross-marker dependencies that could be captured by conditioning the feature extractor itself.

Foundation-model trends for multiplex imaging. Large-scale self-supervised pretraining (Bommansani et al., 2021) has enabled transferable visual representations via masked prediction (Kraus et al., 2024; Wenckstern et al., 2025) or self-supervised distillation objectives (Oquab et al., 2024). For multiplex imaging, self-supervision is attractive because heterogeneous collections can be exploited without dense per-marker labels. However, as IMC introduces modality-specific artifacts (e.g., hot pixels and ion-counting noise); a recent self-supervised foundation model for spatial proteomics, KRONOS, explicitly excludes ion-based modalities such as IMC from training and notes that they may require architectural modifications or modality-specific adaptation strategies (Shaban et al., 2025).

3. Methodology

3.1. ImmuVis architecture

Let $\mathcal{M} = \{m_1, \dots, m_N\}$ denote the global pan-cohort marker vocabulary. Given two *ordered* marker sets $\mathcal{I}_e, \mathcal{J}_d \subset \mathcal{M}$, indexed as $\mathcal{I}_e = (i^1, \dots, i^{C_e})$ and $\mathcal{J}_d = (j^1, \dots, j^{C_d})$, with $C_e = |\mathcal{I}_e|$ and $C_d = |\mathcal{J}_d|$, ImmuVis instantiates a marker-specific encoder-decoder pair.

$$\text{ImmuVis}(\mathcal{I}_e, \mathcal{J}_d) = (\text{Enc}^{\mathcal{I}_e}, \text{Dec}^{\mathcal{J}_d}).$$

The encoder $\text{Enc}^{\mathcal{I}_e}$ maps the multiplex image $(\mathbf{X}_{i^1}, \dots, \mathbf{X}_{i^{C_e}}) = \mathbf{X} \in \mathbb{R}^{C_e \times H_0 \times W_0}$, to a pan-marker latent representation $\mathbf{Z} = \text{Enc}^{\mathcal{I}_e}(\mathbf{X}) \in \mathbb{R}^{d_{lat} \times H_{lat} \times W_{lat}}$. The decoder $\text{Dec}^{\mathcal{J}_d}$ maps \mathbf{Z} to image-level point-wise predictions for the markers in \mathcal{J}_d , producing the mean \mathbf{X}^μ and the corresponding log-variance $\mathbf{X}^{\log \sigma^2}$:

$$(\mathbf{X}^\mu, \mathbf{X}^{\log \sigma^2}) = \text{Dec}^{\mathcal{J}_d}(\mathbf{Z}) \in \mathbb{R}^{2 \times C_d \times H_0 \times W_0}.$$

ImmuVis architecture overview is presented in Figure 2.

3.1.1. $\text{Enc}^{\mathcal{I}_e}$ HYPERNETWORK

Given \mathcal{I}_e , the instantiated encoder factors to a composition:

$$\mathbf{Z} = \text{Enc}^{\mathcal{I}_e}(\mathbf{X}) = \text{Enc}_{pm} \circ \mathfrak{H}_e^{\mathcal{I}_e} \circ \text{Enc}_{ma}(\mathbf{X}),$$

where Enc_{ma} is a *marker-agnostic* encoder applied independently per input marker channel, $\mathfrak{H}_e^{\mathcal{I}_e}$ is a *marker-conditional* hyperconvolution operator instantiated from marker embeddings for the input set \mathcal{I}_e , and Enc_{pm} maps the resulting features into a shared *pan-marker* latent space. Formal definitions are provided below.

Marker-agnostic encoding Enc_{ma} . Let $\mathfrak{S} : \mathbb{R}^{1 \times H_0 \times W_0} \rightarrow \mathbb{R}^{d_{ma} \times H_{ma} \times W_{ma}}$ be a convolutional *stem* shared across markers, where d_{ma} is the marker-agnostic feature width. \mathfrak{S} preprocesses each marker-channel independently, downsampling the image while capturing

local spatial expression patterns. Applying \mathfrak{S} to each marker channel and concatenating along the channel axis yields $\text{Enc}_{ma} : \mathbb{R}^{C_e \times H_0 \times W_0} \rightarrow \mathbb{R}^{C_e \cdot d_{ma} \times H_{ma} \times W_{ma}}$ given as:

$$\mathbf{W} = \text{Enc}_{ma}(\mathbf{X}) = [\mathfrak{S}(\mathbf{X}_{i^1}); \dots; \mathfrak{S}(\mathbf{X}_{i^{C_e}})]_0$$

providing compressed, marker-agnostic representation \mathbf{W} of \mathbf{X} . Here $[\cdot; \cdot]_k$ denotes the concatenation along the k -th dimension.

Encoder Hyperconvolution operator \mathfrak{H}_e .

Let

$$\phi_e : \mathcal{M} \rightarrow \mathbb{R}^{d_{pm} \times d_{ma} \times h_e \times w_e},$$

be a learnable marker-conditional convolutional kernel generator, where d_{pm} is the channel width of the pan-marker space, and (h_e, w_e) is the spatial kernel size. For \mathcal{I}_e , we formulate a hyperkernel $\mathbf{H}_e^{\mathcal{I}_e} \in \mathbb{R}^{d_{pm} \times C_e \cdot d_{ma} \times h_e \times w_e}$ as:

$$\mathbf{H}_e^{\mathcal{I}_e} = [\phi_e(i^1); \dots; \phi_e(i^{C_e})]_1.$$

Then $\mathfrak{H}_e^{\mathcal{I}_e} : \mathbb{R}^{C_e \cdot d_{ma} \times H_{ma} \times W_{ma}} \rightarrow \mathbb{R}^{d_{pm} \times H_{pm} \times W_{pm}}$ is a single dynamic convolution operator (Li & Yao, 2024; Chen et al., 2020):

$$\mathbf{V} = \mathfrak{H}_e^{\mathcal{I}_e}(\mathbf{W}) = \mathbf{W} \otimes_{s,p} \mathbf{H}_e^{\mathcal{I}_e},$$

where $\otimes_{s,p}$ is a standard 2D convolution operation with stride s and padding p , and H_{pm} and W_{pm} are the output spatial dimensions. Now \mathbf{V} is an embedding of \mathbf{X} into a unified pan-marker representation. Since $\mathfrak{H}_e^{\mathcal{I}_e}$ depends on \mathcal{I}_e , the induced hyperkernel adapts to the observed markers and enables capturing fine-grained local cross-marker dependencies.

Pan-marker backbone Enc_{pm} . Since \mathbf{V} is a universal, fixed-sized embedding, it enables the application of standard computer vision backbones. Specifically, $\text{Enc}_{pm} : \mathbb{R}^{d_{pm} \times H_{pm} \times W_{pm}} \rightarrow \mathbb{R}^{d_{lat} \times H_{lat} \times W_{lat}}$ is any fixed-channel vision backbone. This choice lets us leverage advances in general-purpose vision models while remaining flexible to arbitrary marker combinations, producing the pan-marker latent representation:

$$\mathbf{Z} = \text{Enc}_{pm}(\mathbf{V}).$$

3.1.2. $\text{Dec}^{\mathcal{J}_d}$ HYPERNETWORK

Analogously to the encoding procedure, given target marker-set specific \mathcal{J}_d , the instantiated decoder $\text{Dec}^{\mathcal{J}_d}$ is a composition:

$$\mathbf{X}^\mu, \mathbf{X}^{\log \sigma^2} = \text{Dec}^{\mathcal{J}_d}(\mathbf{Z}) = \text{Dec}_{ma} \circ \mathfrak{H}_d^{\mathcal{J}_d}(\mathbf{Z}),$$

where $\mathfrak{H}_d^{\mathcal{J}_d}$ is a *marker-conditioned* hyperconvolution that maps the latent representation to *marker-specific* decoding features, and Dec_{ma} produces per-marker mean predictions and log-variance for markers in \mathcal{J}_d . Formal definitions are provided below.

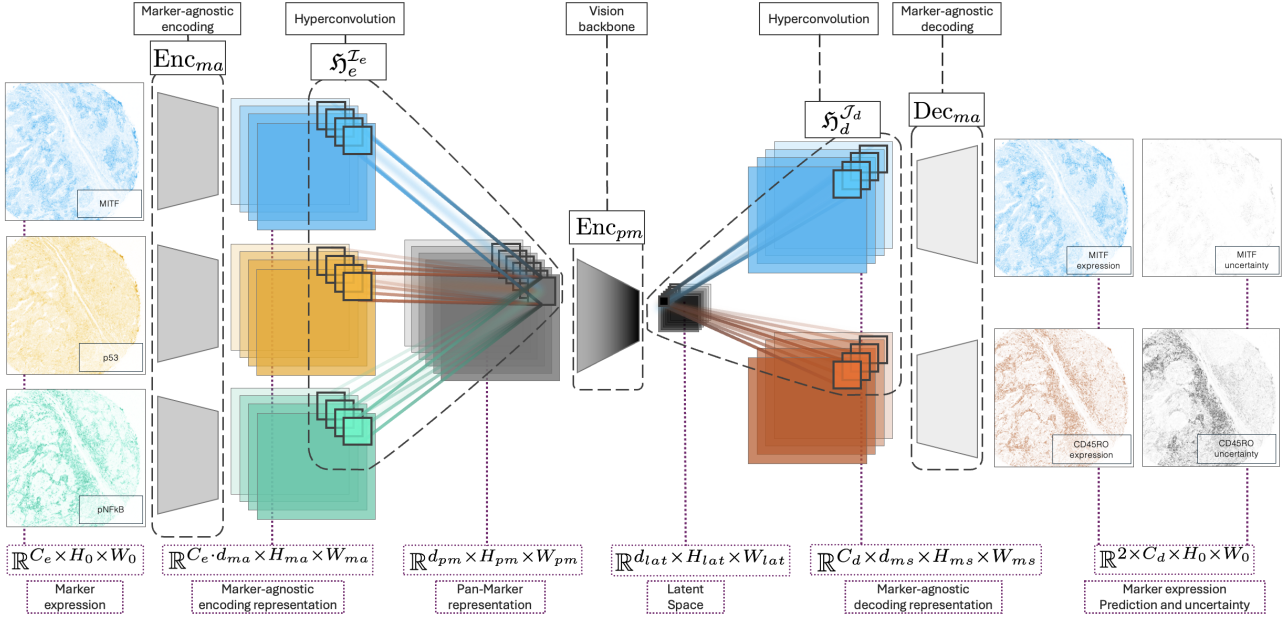


Figure 2. ImmuVis architecture overview. Marker-agnostic encoder stems embed each input marker channel and a hyperconvolution module, conditioned on learned marker embeddings, fuses them into a shared pan-marker representation processed by a standard vision backbone. A symmetric hyperconvolution and marker-agnostic decoder instantiates the requested output marker set, predicting per-marker reconstructions together with pixel-wise uncertainty (heteroscedastic log-variance).

Decoder Hyperconvolution operator \mathfrak{H}_d .

$$\phi_d : \mathcal{M} \rightarrow \mathbb{R}^{d_{\text{ms}} \times d_{\text{lat}} \times h_d \times w_d},$$

be a learnable marker-conditional convolutional kernel generator, where d_{ms} is the width of the marker set specific decoder space, and (h_d, w_d) is the spatial kernel size. We define $\mathfrak{H}_d^{\mathcal{J}_d} : \mathbb{R}^{d_{\text{lat}} \times H_{\text{lat}} \times W_{\text{lat}}} \rightarrow \mathbb{R}^{C_d \times d_{\text{ms}} \times H_{\text{ms}} \times W_{\text{ms}}}$ as:

$$\mathbf{U} = \mathfrak{H}_d^{\mathcal{J}_d}(\mathbf{Z}) = [\mathbf{Z} \otimes_{s,p} \phi_d(j^1); \dots; \mathbf{Z} \otimes_{s,p} \phi_d(j^{C_d})]^0$$

where $\mathbf{U} = (\mathbf{U}_{j^1}, \dots, \mathbf{U}_{j^{C_d}})$ constitutes an embedding of a latent space \mathbf{Z} into a marker set specific space. Here $[\cdot; \cdot]^k$ denotes stacking along the k -th dimension.

Marker-agnostic decoding Dec_{ma} . Let $\mathfrak{R} : \mathbb{R}^{d_{\text{ms}} \times H_{\text{ms}} \times W_{\text{ms}}} \rightarrow \mathbb{R}^{2 \times H_0 \times W_0}$, be a convolutional head operator, that provides marker predictions and uncertainties from a marker-specific representations. $\text{Dec}_{\text{ma}} : \mathbb{R}^{C_d \times d_{\text{ms}} \times H_{\text{ms}} \times W_{\text{ms}}} \rightarrow \mathbb{R}^{2 \times C_d \times H_0 \times W_0}$ applies \mathfrak{R} to each marker channel independently and stacks the results:

$$\hat{\mathbf{X}} = \text{Dec}_{\text{ma}}(\mathbf{U}) = [\mathfrak{R}(\mathbf{U}_{j^1}); \dots; \mathfrak{R}(\mathbf{U}_{j^{C_d}})]^1.$$

Finally, we set $\mathbf{X}^{\mu} = \hat{\mathbf{X}}^0$ and $\mathbf{X}^{\log \sigma^2} = \hat{\mathbf{X}}^1$ to obtain the final point-wise prediction and its uncertainty approximation for markers from \mathcal{J}_d , respectively.

3.2. Masked Modelling Task

We train ImmuVis with a masked modelling objective (He et al., 2022). Let $\mathbf{X}_{\mathcal{A}}$ denote an multiplexed image \mathbf{X} restricted only to markers from marker set \mathcal{A} . During the training, for each image $\mathbf{X}_{\mathcal{I}_{\text{img}}} \in \mathbb{R}^{C_{\text{img}} \times H \times W}$ with a marker set \mathcal{I}_{img} we: (i) sample a target marker set $\mathcal{I}_{\text{tgt}} \subseteq \mathcal{I}_{\text{img}}$, (ii) sample an input marker set $\mathcal{I}_{\text{in}} \subseteq \mathcal{I}_{\text{tgt}}$, and (iii) apply patch-wise spatial masking on $\mathbf{X}_{\mathcal{I}_{\text{in}}}$ to obtain a masked input $\tilde{\mathbf{X}}_{\mathcal{I}_{\text{in}}}$. $\tilde{\mathbf{X}}_{\mathcal{I}_{\text{in}}}$ is then fed to a model to obtain unmasked point-wise predictions and uncertainty estimations on a marker set \mathcal{I}_{tgt} :

$$(\mathbf{X}_{\mathcal{I}_{\text{tgt}}}^{\mu}, \mathbf{X}_{\mathcal{I}_{\text{tgt}}}^{\log \sigma^2}) = \text{ImmuVis}(\mathcal{I}_{\text{in}}, \mathcal{I}_{\text{tgt}}) (\tilde{\mathbf{X}}_{\mathcal{I}_{\text{in}}}).$$

At test time, we set $\mathcal{I}_{\text{tgt}} = \mathcal{I}_{\text{img}}$. For detailed procedures of sampling and masking see Appendix A.1.

Loss function We train ImmuVis using a Gaussian heteroscedastic regression scheme (Stirn et al., 2022). It assumes that each element $\mathbf{X}_{c,h,w}$ of a target image $\mathbf{X}_{\mathcal{I}_{\text{tgt}}}$ follows an independent Gaussian distribution:

$$\mathbf{X}_{c,h,w} \sim \mathcal{N}(\mathbf{X}_{c,h,w}^{\mu}, \exp(\mathbf{X}_{c,h,w}^{\log \sigma^2})).$$

Then the training objective is, up to an additive constant, the Gaussian negative log-likelihood given by (Stirn et al.,

2022):

$$\hat{\ell} = \text{clamp}(\mathbf{X}_{\mathcal{I}_{\text{tgt}}}^{\log \sigma^2}), \quad \epsilon = 10^{-8},$$

$$\mathcal{L}_{\text{nll}} = \text{mean} \left(\frac{(\mathbf{X}_{\mathcal{I}_{\text{tgt}}} - \mathbf{X}_{\mathcal{I}_{\text{tgt}}}^{\mu})^2}{\exp(\hat{\ell}) + \epsilon} + \hat{\ell} \right),$$

where the mean is taken over the batch, channels, and spatial dimensions. The log-variance $\hat{\ell}$ is stabilized using a gradient-preserving clamp to improve training stability. For implementation details see Appendix A.2.

4. Results

4.1. IMC17M dataset

To train ImmuVis, we curated IMC17M, the largest IMC corpus reported to date, composed of 17M patches from 28 datasets spanning 25 unique marker panels (24,405 images and 265 markers) across 14 histologies. For more details about IMC17M see Appendix A.3 Table 4. For training we split images into train/test in a 4:1 ratio, stratifying by dataset panel to preserve panel- and histopathology-level representation. All patches derived from the same parent image were assigned to the same split to prevent patch-level leakage.

Preprocessing Overview For training, we preprocess raw IMC images with variance-stabilizing transformation, frequency-based denoising, and intensity normalization, and then train/evaluate on fixed-size crops with standard spatial augmentations; full procedural details and all preprocessing parameters are given in Appendix A.4.

4.2. ImmuVis models

ImmuVis is a fully convolutional model in which all sub-networks (\mathfrak{S} , Enc_{pm} , and \mathfrak{R}) use a ConvNeXt v2 backbone (Woo et al., 2023), with a pan-marker latent dimension $d_{\text{lat}} = 768$. To analyze the influence of architecture choice of Enc_{pm} we also consider a ViT-based variant $\text{ImmuVis}_{\text{ViT}}$ with a ViT-M backbone (Dosovitskiy et al., 2021), selected to match latent dimensionality of both models. For details of architectures of both models see Appendix A.5.

We trained both models for 200 epochs with AdamW (Loshchilov & Hutter, 2019) optimizer using weight decay 10^{-4} and a cosine annealing learning-rate schedule with linear warmup (for full details see Appendix A.6). As shown in Table 1, ConvNeXt v2 achieves lower MAE and MSE on the test set, indicating that preserving local spatial detail with convolutional processing is advantageous for masked modelling task.

Table 1. Test set result comparison for ImmuVis and $\text{ImmuVis}_{\text{ViT}}$. We report latent dimensionality, and MAE/MSE loss for Masked Modelling task

Model	Latent Dim.	MAE	MSE
ImmuVis	768	0.0234	0.0028
$\text{ImmuVis}_{\text{ViT}}$	768	0.0258	0.0032

4.3. Experiments

We comprehensively evaluate ImmuVis and $\text{ImmuVis}_{\text{ViT}}$ across (i) virtual staining and uncertainty estimation fidelity, (ii) representation learning for celltyping and clinical prediction tasks, and (iii) computational efficiency, benchmarking against VirTues (Wenckstern et al., 2025), a prior state-of-the-art method that was shown to outperform baseline methods (Kraus et al., 2024; Shaban et al., 2025; Sorin et al., 2023) on these tasks. For VirTues, we use the publicly released pretrained checkpoint provided by the authors on Hugging Face¹.

4.3.1. VIRTUAL STAINING

Setup. To evaluate virtual staining quality in an out-of-cohort setting, we use the IMMUCan Head & Neck cohort (743 images), which was not included in the VirTues training data. We train *zero-shot* variants of ImmuVis and $\text{ImmuVis}_{\text{ViT}}$ on IMC17M after excluding this cohort. For a fair comparison, we restrict evaluation to the $M = 38$ markers shared with the VirTues training panel and apply the same preprocessing as in the original VirTues work.

For each test image, we predict all M target markers in a leave-one-marker-out manner and compute pixel-level errors (MSE); we then average these within each image to obtain an image-level score for each marker. We report the distribution of image-level scores across the cohort, assess paired differences between methods using the Wilcoxon signed-rank test, and control the false discovery rate across markers using the Benjamini-Hochberg procedure.

Data overlap. We note that 14 Head & Neck images in our evaluation set are included in the Eling et al. dataset (Eling et al., 2025) used during VirTues pretraining and may therefore have been seen by VirTues during training; consequently, our comparison on these samples is conservative with respect to VirTues.

Results. As presented in Figure 3, on the full Head & Neck cohort, both ImmuVis and $\text{ImmuVis}_{\text{ViT}}$ consistently outperform VirTues, achieving significantly lower MSE for every evaluated markers ($q < 10^{-4}$, FDR-corrected). Com-

¹<https://huggingface.co/bunnelab/virtues>, snapshot as of Dec 9, 2025 commit

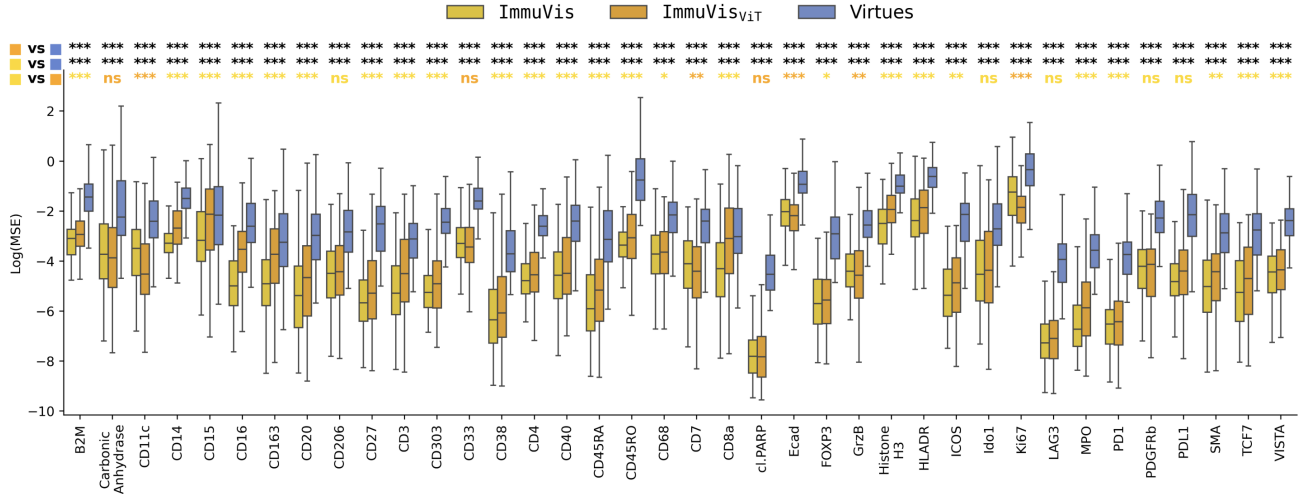


Figure 3. Quantitative virtual staining evaluation on the Head & Neck cohort. Per-marker reconstruction accuracy measured by image-level log(MSE) for ImmuVis, ImmuVis_{ViT}, and VirTues. Each boxplot summarizes the distribution of image-level scores, where each image score is obtained by averaging patch-level errors over all patches from that image. The three rows above the plot report paired Wilcoxon signed-rank tests results across images for the corresponding model pairs (as indicated in the left top corner), with significance after FDR correction (ns - not significant; (*) < 0.05; (**) < 0.01; (***) < 0.001).

paring `ImmuVis` to `ImmuVisViT`, `ImmuVisViT` performs significantly better on five markers, the two methods are not significantly different on eight markers, and `ImmuVis` achieves the best performance with a statistically significant margin on the remaining 25 markers. Additionally, as illustrated in Figure 4, the better out of two, `ImmuVis`, produces qualitatively faithful reconstructions under masking and in the zero-shot setting, better preserving tissue morphology and local spatial structure than `VirTues` across representative markers (CD45RO, HLADR, H3). Importantly, lower quality reconstruction are supported by high uncertainty maps discussed in the following section.

4.3.2. UNCERTAINTY ESTIMATION

Setup. To quantify estimation uncertainty fidelity, we leverage the heteroscedastic Gaussian head of `ImmuVis`, which outputs a per-pixel mean μ and log-variance $\log \sigma^2$ for each reconstructed channel. We evaluate whether the predicted uncertainty is reliably *calibrated* in the sense of tracking reconstruction error. We perform this analysis separately for active (observed) channels and masked (held-out) channels, and for `ImmuVis` trained on a full IMC17M and the *zero-shot* variant.

Results. Figure 5 shows a strong positive association between predicted uncertainty and reconstruction error across pixels, evidenced by high correlations between $\log \sigma^2$ and $\log(\text{MAE})$ for both considered settings. Importantly, this trend holds not only for active channels ($r_{\text{act}} = 0.962$ and 0.96, for *full* and *zero-shot*, respectively), where the task

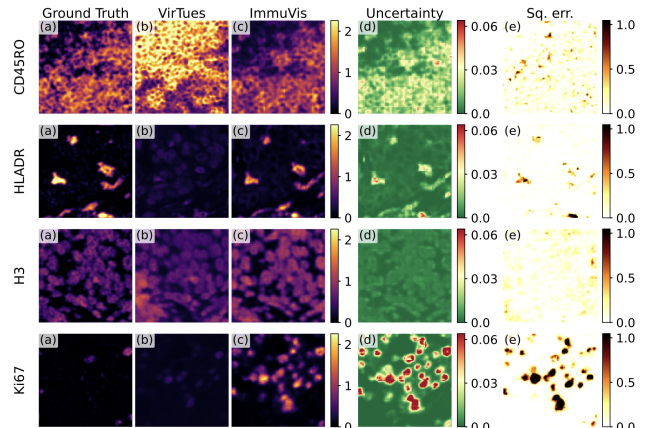


Figure 4. Qualitative virtual staining results under masking and zero-shot settings. Representative patches from Head and Neck cohort (IMMUCAN Consortium, 2025) for four markers (CD45RO, HLA DR, H3, Ki67). Columns show the Ground Truth channel, Reconstruction by VirTues and ImmuVis in leave-one-out setting, prediction uncertainty σ^2 map, and squared error $(\mathbf{X}_c^\mu - \mathbf{X}_c)^2$. ImmuVis preserves spatial structure and produces coherent zero-shot reconstructions, with uncertainty highlighting lower-confidence regions (see Ki67 example).

is genuinely an imputation, but also for masked channels ($r_{\text{mask}} = 0.943$ and 0.93 , for *full* and *zero-shot*, respectively), indicating that the uncertainty head captures local ambiguity in the reconstruction rather than merely reflecting the masking pattern. Moreover, qualitatively, as presented in the Figure 4, in the Ki67 zero-shot example, uncertainty maps effectively capture regions where reconstructions are inadequate. Together, these results confirm that ImmuVis's

heteroscedastic output provides a meaningful per-pixel confidence signal that generalizes from the full setting to the more challenging zero-shot regime.

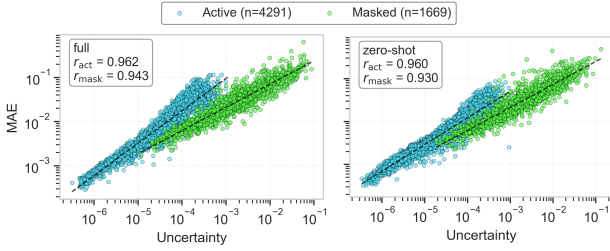


Figure 5. MAE vs uncertainty correlation for marker reconstruction. Scatter plots on log-log scale for *full* (left) and *zero-shot* (right) ImmuVis models; trained with and without Head and Neck cohort, respectively (IMMUcan Consortium, 2025). Active channels (blue, $n = 4291$) and Masked channels (green, $n = 1669$) both show strong positive correlation between prediction error and uncertainty for all cases. Dashed lines show linear regression fits.

4.4. Representation Learning: Cell Typing

Setup To evaluate the quality of single-cell representations learned by the three models, we use the IMC dataset of Eling et al. (Eling et al., 2025), which provides expert-curated manual cell-type annotations. Single-cell extraction and embedding construction are described in Appendix A.7. We train a multinomial logistic regression *linear probe* on frozen single-cell embeddings to predict cell type, and report per-cell-type F1 scores with confidence intervals obtained via 10-fold cross-validation. To compare methods, we test paired per-fold performance differences using the Wilcoxon signed-rank test and control the false discovery rate across cell types using the Benjamini-Hochberg procedure.

Results The overall cell typing performance of linear probes trained on frozen embeddings is presented in Figure 6. Both ImmuVis and ImmuVis_{ViT} outperform the baseline VirTues across all 14 evaluated cell types, with significantly higher F1 scores after FDR correction ($q < 10^{-4}$). Comparing ImmuVis to ImmuVis_{ViT}, ImmuVis_{ViT} performs significantly better on four cell types, the two methods are not significantly different on four cell types, and ImmuVis achieves significantly better performance on the remaining six cell types. Overall, these results indicate that hyperconvolution-based embeddings provide very strong single-cell representations for cell typing task.

4.5. Representation Learning: Clinical predictions

Setup We further evaluate whether ImmuVis learns representations that transfer to patient-level clinical prediction. We consider two published IMC cohorts with clinical labels (Danenbergs et al., 2022; Cords et al., 2024) and assess

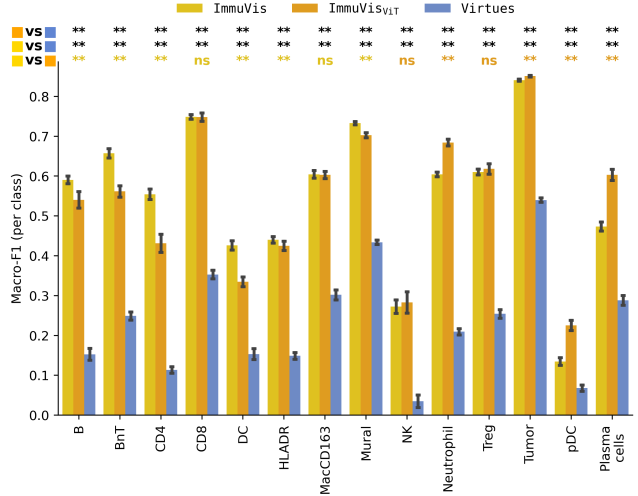


Figure 6. Cell-typing performance from learned representations. Bars show mean F1 across cross-validation folds with confidence intervals (whiskers), higher is better. The three rows above the plot report paired Wilcoxon signed-rank tests on per-fold scores for the corresponding model pairs (as indicated in the left top corner), with significance after FDR correction (ns - not significant; (*) < 0.05 ; (**) < 0.01 ; (***) < 0.001).

whether frozen embeddings support downstream classification under simple linear probing as well as gated attention-based multiple instance learning model (abMIL) (Ilse et al., 2018). For each cohort, we extract patch embeddings from the frozen ImmuVis encoder (no fine-tuning). We aggregate patch embeddings to the patient level by mean pooling, report Macro-F1 across cross-validation splits and summarize results as mean \pm standard deviation. We compare to VirTues (Wenckstern et al., 2025) under the same protocol.

Results Table 2 summarizes Macro-F1 score across clinical endpoints in both cohorts in question. ImmuVis achieves the best average performance in the majority of tasks for both considered classification strategies (5/7 and 6/7 for Linear Regression and abMIL, respectively). VirTues, consistently provides better results in Cancer Subtype prediction for (Cords et al., 2024) cohort, independently of classification strategy. Despite this fact, these results support the claim that operator-level conditioning during pretraining yields embeddings that remain informative also for clinically relevant prediction tasks with minimal downstream supervision.

4.6. Computational efficiency

Setup. We compare inference-time computational cost of ImmuVis, ImmuVis_{ViT}, and VirTues on a single forward pass for an IMC crop of shape [40, 128, 128]. All measurements are obtained on an NVIDIA H100 GPU using

Table 2. Representation learning for clinical endpoints (Macro-F1; higher is better). Values report mean \pm std Macro-F1 across 10-fold cross-validation; best performance per endpoint is shown in bold.

Model	Pred.	(Danenberg et al., 2022)				(Cords et al., 2024)		
		PAM50	Grade	ER Status	ERBB2	Cancer Subtype	Relapse	Grade
VirTues	LR	0.42\pm0.08	0.46 \pm 0.05	0.77 \pm 0.06	0.64 \pm 0.15	0.81\pm0.04	0.56 \pm 0.05	0.49 \pm 0.08
ImmuVis _{ViT}	LR	0.27 \pm 0.07	0.46 \pm 0.05	0.47 \pm 0.05	0.47 \pm 0.00	0.73 \pm 0.03	0.50 \pm 0.04	0.42 \pm 0.02
ImmuVis	LR	0.42 \pm 0.06	0.46\pm0.03	0.78\pm0.06	0.79\pm0.11	0.80 \pm 0.04	0.58\pm0.05	0.50\pm0.07
VirTues	abMIL	0.42 \pm 0.06	0.48 \pm 0.04	0.77 \pm 0.09	0.66 \pm 0.10	0.83\pm0.02	0.58 \pm 0.03	0.50 \pm 0.04
ImmuVis _{ViT}	abMIL	0.42 \pm 0.04	0.45 \pm 0.02	0.69 \pm 0.09	0.77 \pm 0.2	0.80 \pm 0.03	0.56 \pm 0.05	0.48 \pm 0.03
ImmuVis	abMIL	0.45\pm0.05	0.49\pm0.05	0.79\pm0.09	0.85\pm0.11	0.82 \pm 0.01	0.61\pm0.05	0.50\pm0.04

100 random inputs; we report parameter count, GFLOPs, mean \pm std execution time (seconds), and peak activation memory (GB).

Results. Table 3 shows that ImmuVis achieves a favorable efficiency-accuracy trade-off. While VirTues incurs high compute cost (1049.3 GFLOPs) and the slowest runtime (244 \pm 2.3 s), both ImmuVis and ImmuVis_{ViT} operate in a substantially lower-compute regime (90.1 and 106.1 GFLOPs, respectively) with markedly faster execution (68 \pm 4.1 s and 63.3 \pm 1.7 s). Compared to ImmuVis_{ViT}, ImmuVis, despite being slightly slower (on average 68s vs 63.3s), reduces parameters (56M vs. 121M) and GFLOPs (90.1 vs. 106.1), and lowers peak activation memory (0.85 GB vs. 1.45 GB), while retaining the fully convolutional scaling of its operators. Interestingly, despite being over 3.5 times faster, ImmuVis reaches 2.65 times larger, but still manageable, peak activation memory usage. Crucially, this footprint is maintained under variable-input operation: the marker-agnostic and hyperconvolution components scale linearly with the number of available markers, without padding to a fixed panel.

Table 3. Computational efficiency comparison. We report the inference cost of ImmuVis, ImmuVis_{ViT}, and VirTues: parameter count, GFLOPs, avarage and standard deviation of execution time [s], and peak activation memory [GB] measured on 100 random inputs of shape: [40, 128, 128].

Model	Params	GFLOPs	Time	Mem.
ImmuVis _{ViT}	121M	106.1	63.3 \pm 1.7	1.45
ImmuVis	56M	90.1	68 \pm 4.1	0.85
VirTues	42.5M	1049.3	244 \pm 2.3	0.32

5. Discussion

ImmuVis addresses a central practical constraint of IMC, namely the absence of a fixed channel marker space, by introducing marker-adaptive hyperconvolutions that generate convolutional kernels from learned marker embeddings. Such design enables a single foundation model to operate

on arbitrary measured marker subsets without re-training. Across virtual staining and multiple representation learning benchmarks, ImmuVis achieves consistent improvements over VirTues, including strong zero-shot performance on unseen panels. On top of that, fully-convolutional ImmuVis consistently outperformed its transformer-based alternative ImmuVis_{ViT}. We attribute this strong performance gains across tasks to a natural property of convolutional models, which can easily preserve local spatial contexts and capture short-range dependencies that are crucial to understand tissue architecture and cellular interaction. Beyond that, the heteroscedastic objective provides per-pixel uncertainty estimates that closely track reconstruction error, offering a practical reliability signal for downstream use (e.g., prioritizing regions or markers requiring caution).

While the proposed design is computationally efficient and cohort-deployable, several limitations remain. First, the training distribution is constrained by marker availability and dataset bias; rare biomarkers and under-represented tissue contexts may yield less reliable reconstructions, especially under zero-shot extrapolation. Second, our likelihood model assumes conditional independence across pixels and channels, which is a pragmatic approximation but may under-represent structured noise or cross-channel dependencies in IMC.

Future work could extend ImmuVis to additional multiplex modalities (e.g., MIBI, CODEX), incorporate richer priors or structured uncertainty (e.g., spatially correlated noise), and develop whole-slide and patient-level pipelines that directly exploit ImmuVis embeddings for clinical endpoints. An additional direction is to analyze and interpret the learned latent representations to better characterize cross-marker dependencies, moving toward more explainable and mechanistically interpretable multiplex-imaging models. Overall, our results suggest that operator-level channel adaptivity is an effective recipe for building practical foundation models in multiplex imaging, combining panel flexibility, efficiency, and reliability-aware predictions within a single architecture.

Impact Statement

Our work advances machine learning for biomedical imaging by introducing a panel-flexible foundation model for imaging mass cytometry (IMC) that can support large-scale spatial proteomics analysis across heterogeneous marker panels, enable cost-effective virtual staining for retrospective and cross-study comparisons, and provide uncertainty estimates that help users interpret predictions responsibly. These capabilities may accelerate biomarker discovery and the development of downstream diagnostic tools, potentially reducing experimental costs and improving clinical decision support, but they require rigorous validation across diverse tissues and clinical settings prior to deployment. As with other medical-imaging models, responsible use also depends on careful handling of sensitive data and proactive assessment of dataset biases that may affect underrepresented populations; to promote transparency and community scrutiny, we plan to release code and pretrained weights.

Acknowledgements

The IMMUCan project has received funding from the Innovative Medicines Initiative 2 Joint Undertaking under grant agreement no. 821558. This Joint Undertaking receives support from the European Union's Horizon 2020 Research and Innovation Programme and EFPIA 24 perpetuity (<https://IMI.europa.eu>).

As a part of SPACETIME consortium, this project has received funding from the European Union's Horizon Europe research and innovation programme under grant agreement No 101136552.

Merck Healthcare KGaA provides funding for the research group.

References

Ajaib, S., Winter-Luke, J., Digby, R. J., Pollock, S., Hemmings, G., Gusnanto, A., Chakrabarty, A., Ismail, A., Wilson, E., Hunter, B., Filby, A., McDonald, D., Brockman, A. A., Ihrie, R. A., and Stead, L. F. Spatial profiling of longitudinal glioblastoma reveals consistent changes in cellular architecture, post-treatment. *Neuro-Oncology*, September 2025. ISSN 1523-5866. doi: 10.1093/neuonc/noaf190. URL <http://dx.doi.org/10.1093/neuonc/noaf190>.

Bao, Y., Sivanandan, S., and Karaletsos, T. Channel vision transformers: An image is worth 1 x 16 x 16 words. In *The Twelfth International Conference on Learning Representations*, 2024. URL <https://openreview.net/forum?id=CK5Hfb5hBG>.

Bendall, S. C., Nolan, G. P., Roederer, M., and Chat- topadhyay, P. K. A deep profiler's guide to cytometry. *Trends in Immunology*, 33(7):323–332, 2012. doi: 10.1016/j.it.2012.02.010.

Bollhagen, A. and Bodenmiller, B. Highly multiplexed tissue imaging in precision oncology and translational cancer research. *Cancer Discovery*, 14(11):2071–2088, November 2024. ISSN 2159-8290. doi: 10.1158/2159-8290.cd-23-1165. URL <http://dx.doi.org/10.1158/2159-8290.CD-23-1165>.

Bommasani, R., Hudson, D. A., Adeli, E., Altman, R., Arora, S., von Arx, S., Bernstein, M. S., Bohg, J., Bosslut, A., Brunskill, E., Brynjolfsson, E., Buch, S., Card, D., Castellon, R., Chatterji, N. S., Chen, A., Creel, K., Davis, J. Q., Demszky, D., Donahue, C., Doumbouya, M., Durmus, E., Ermon, S., Etchemendy, J., Ethayarajh, K., Fei-Fei, L., Finn, C., Gale, T., Gillespie, L., Goel, K., Goodman, N., Grossman, S., Guha, N., Hashimoto, T., Henderson, P., Hewitt, J., Ho, D. E., Hong, J., Hsu, K., Huang, J., Icard, T., Jain, S., Jurafsky, D., Kalluri, P., Karamcheti, S., Keeling, G., Khani, F., Khattab, O., Koh, P. W., Krass, M., Krishna, R., Kuditipudi, R., Kumar, A., Ladhak, F., Lee, M., Lee, T., Leskovec, J., Levent, I., Li, X. L., Li, X., Ma, T., Malik, A., Manning, C. D., Mirchandani, S., Mitchell, E., Munyikwa, Z., Nair, S., Narayan, A., Narayanan, D., Newman, B., Nie, A., Niebles, J. C., Nilforoshan, H., Nyarko, J., Ogut, G., Orr, L., Papadimitriou, I., Park, J. S., Piech, C., Portelance, E., Potts, C., Raghunathan, A., Reich, R., Ren, H., Rong, F., Roohani, Y. H., Ruiz, C., Ryan, J., Ré, C., Sadigh, D., Sagawa, S., Santhanam, K., Shih, A., Srinivasan, K. P., Tamkin, A., Taori, R., Thomas, A. W., Tramèr, F., Wang, R. E., Wang, W., Wu, B., Wu, J., Wu, Y., Xie, S. M., Yasunaga, M., You, J., Zaharia, M., Zhang, M., Zhang, T., Zhang, X., Zhang, Y., Zheng, L., Zhou, K., and Liang, P. On the opportunities and risks of foundation models. *ArXiv*, 2021. URL <https://crfm.stanford.edu/assets/report.pdf>.

Bowen, C. M., Deng, N., Reyes-Uribe, L., Parra, E. R., Rocha, P., Solis, L. M., Wistuba, I. I., Sepeda, V. O., Vornik, L., Perloff, M., Szabo, E., Umar, A., Sinha, K. M., Brown, P. H., and Vilar, E. Naproxen chemoprevention induces proliferation of cytotoxic lymphocytes in lynch syndrome colorectal mucosa. *Frontiers in Immunology*, 14, May 2023. ISSN 1664-3224. doi: 10.3389/fimmu.2023.1162669. URL <http://dx.doi.org/10.3389/fimmu.2023.1162669>.

Bussi, Y. and Keren, L. Multiplexed image analysis: what have we achieved and where are we headed? *Nature Methods*, 21(12):2212–2215, December 2024. ISSN 1548-7105. doi: 10.1038/s41592-024-02539-5. URL <http://dx.doi.org/10.1038/s41592-024-02539-5>.

Butterworth, S. On the Theory of Filter Amplifiers. *Experimental Wireless & the Wireless Engineer*, 7:536–541, October 1930.

Chang, Q., Ornatsky, O. I., Siddiqui, I., Loboda, A., Baranov, V. I., and Hedley, D. W. Imaging mass cytometry. *Cytometry Part A*, 91(2):160–169, February 2017. ISSN 1552-4930. doi: 10.1002/cyto.a.23053. URL <http://dx.doi.org/10.1002/cyto.a.23053>.

Chen, Y., Dai, X., Liu, M., Chen, D., Yuan, L., and Liu, Z. Dynamic convolution: Attention over convolution kernels, 2019. URL <https://arxiv.org/abs/1912.03458>.

Chen, Y., Dai, X., Liu, M., Chen, D., Yuan, L., and Liu, Z. Dynamic convolution: Attention over convolution kernels. In *Proceedings of the IEEE/CVF Conference on Computer Vision and Pattern Recognition (CVPR)*, June 2020.

Chevrier, S., Crowell, H. L., Zanotelli, V. R. T., Engler, S., Robinson, M. D., and Bodenmiller, B. Compensation of signal spillover in suspension and imaging mass cytometry. *Cell Systems*, 6(5):612–620.e5, 2018. doi: 10.1016/j.cels.2018.02.010.

Cho, Y., Lee, J. W., Shin, S. M., Hernandez, A. G., Yuan, X., Schneider, J., Hooper, J. E., Wood, L. D., Jaffee, E. M., Deshpande, A., and Ho, W. J. Modeling cellular influence delineates functionally relevant cellular neighborhoods in primary and metastatic pancreatic ductal adenocarcinoma. *BiorXiv*, June 2025. doi: 10.1101/2025.06.12.659314. URL <http://dx.doi.org/10.1101/2025.06.12.659314>.

Cords, L., Tietscher, S., Anzeneder, T., Langwieder, C., Rees, M., de Souza, N., and Bodenmiller, B. Cancer-associated fibroblast classification in single-cell and spatial proteomics data. *Nature Communications*, 14(1), July 2023. ISSN 2041-1723. doi: 10.1038/s41467-023-39762-1. URL <http://dx.doi.org/10.1038/s41467-023-39762-1>.

Cords, L., Engler, S., Haberecker, M., Rüschoff, J. H., Moch, H., de Souza, N., and Bodenmiller, B. Cancer-associated fibroblast phenotypes are associated with patient outcome in non-small cell lung cancer. *Cancer Cell*, 42(3):396–412.e5, March 2024. ISSN 1535-6108. doi: 10.1016/j.ccr.2023.12.021. URL <http://dx.doi.org/10.1016/j.ccr.2023.12.021>.

Diamond, N., Engler, S., Zanotelli, V. R., Schapiro, D., Wasserfall, C. H., Kusmartseva, I., Nick, H. S., Thorel, F., Herrera, P. L., Atkinson, M. A., and Bodenmiller, B. A map of human type 1 diabetes progression by imaging mass cytometry. *Cell Metabolism*, 29(3):755–768.e5, March 2019. ISSN 1550-4131. doi: 10.1016/j.cmet.2018.11.014. URL <http://dx.doi.org/10.1016/j.cmet.2018.11.014>.

Danenberg, E., Bardwell, H., Zanotelli, V. R. T., Provenzano, E., Chin, S.-F., Rueda, O. M., Green, A., Rakha, E., Aparicio, S., Ellis, I. O., Bodenmiller, B., Caldas, C., and Ali, H. R. Breast tumor microenvironment structures are associated with genomic features and clinical outcome. *Nature Genetics*, 54(5):660–669, April 2022. ISSN 1546-1718. doi: 10.1038/s41588-022-01041-y. URL <http://dx.doi.org/10.1038/s41588-022-01041-y>.

de Souza, N., Zhao, S., and Bodenmiller, B. Multiplex protein imaging in tumour biology. *Nature Reviews Cancer*, 24(3):171–191, February 2024. ISSN 1474-1768. doi: 10.1038/s41568-023-00657-4. URL <http://dx.doi.org/10.1038/s41568-023-00657-4>.

Dolezal, J. M., Srisuwananukorn, A., Karpeyev, D., Ramesh, S., Kochanny, S., Cody, B., Mansfield, A. S., Rakshit, S., Bansal, R., Bois, M. C., Bungum, A. O., Schulte, J. J., Vokes, E. E., Garassino, M. C., Hussain, A. N., and Pearson, A. T. Uncertainty-informed deep learning models enable high-confidence predictions for digital histopathology. *Nature Communications*, 13(1), November 2022. ISSN 2041-1723. doi: 10.1038/s41467-022-34025-x. URL <http://dx.doi.org/10.1038/s41467-022-34025-x>.

Dosovitskiy, A., Beyer, L., Kolesnikov, A., Weissenborn, D., Zhai, X., Unterthiner, T., Dehghani, M., Minderer, M., Heigold, G., Gelly, S., Uszkoreit, J., and Houlsby, N. An image is worth 16x16 words: Transformers for image recognition at scale. In *International Conference on Learning Representations*, 2021. URL <https://openreview.net/forum?id=YicbFdNTTy>.

Ehret, B. Imc data associated with the publication 'shaking organoid co-cultures: human-relevant models of epithelial, stromal and immune interactions for cancer research and immunotherapy development', 2025. URL <https://zenodo.org/doi/10.5281/zenodo.15198804>.

Einhaus, J., Gaudilliere, D. K., Hedou, J., Feyaerts, D., Ozawa, M. G., Sato, M., Ganio, E. A., Tsai, A. S., Stelzer, I. A., Bruckman, K. C., Amar, J. N., Sabayev, M., Bonham, T. A., Gillard, J., Diop, M., Cambriel, A., Mihalic, Z. N., Valdez, T., Liu, S. Y., Feirreira, L., Lam, D. K., Sunwoo, J. B., Schürch, C. M., Gaudilliere, B., and Han, X. Spatial subsetting enables integrative modeling of oral squamous cell carcinoma multiplex imaging data. *iScience*, 26(12):108486, December 2023. ISSN 2589-0042. doi: 10.1016/j.isci.2023.108486. URL <http://dx.doi.org/10.1016/j.isci.2023.108486>.

Eling, N., Dorier, J., Rusakiewicz, S., Liechti, R., Devanand, P., Daniel, M., Windhager, J., Fernandez, B. P., Dégliste, S., Despland, L., Benyagoub, A., Mozejko, M., Uchal, D., Szczurek, E., Loboda, A., Sandkuijl, D., Parsotam, N., Hong, H. S., Morfouace, M., Guex, N., Coukos, G., Bodenmiller, B., Tissot, S., and Schulz, D. Multi-modal image analysis for large-scale cancer tissue studies within immucan. *Cell Reports Methods*, 5(9):101170, September 2025. ISSN 2667-2375. doi: 10.1016/j.crmeth.2025.101170. URL <http://dx.doi.org/10.1016/j.crmeth.2025.101170>.

Giesen, C., Wang, H. A. O., Schapiro, D., Zivanovic, N., Jacobs, A., Hattendorf, B., Schüffler, P. J., Grolimund, D., Buhmann, J. M., Brandt, S., Varga, Z., Wild, P. J., Günther, D., and Bodenmiller, B. Highly multiplexed imaging of tumor tissues with subcellular resolution by mass cytometry. *Nature Methods*, 11(4):417–422, March 2014. ISSN 1548-7105. doi: 10.1038/nmeth.2869. URL <http://dx.doi.org/10.1038/nmeth.2869>.

Ha, D., Dai, A. M., and Le, Q. V. Hypernetworks. In *International Conference on Learning Representations*, 2017. URL <https://openreview.net/forum?id=rkpACellx>.

Haley, M. J., Bere, L., Minshull, J., Georgaka, S., Garcia-Martin, N., Howell, G., Coope, D. J., Roncaroli, F., King, A., Wedge, D. C., Allan, S. M., Pathmanaban, O. N., Brough, D., and Couper, K. N. Hypoxia coordinates the spatial landscape of myeloid cells within glioblastoma to affect survival. *Science Advances*, 10(20), May 2024. ISSN 2375-2548. doi: 10.1126/sciadv.adj3301. URL <http://dx.doi.org/10.1126/sciadv.adj3301>.

He, K., Chen, X., Xie, S., Li, Y., Dollar, P., and Girshick, R. Masked autoencoders are scalable vision learners. In *2022 IEEE/CVF Conference on Computer Vision and Pattern Recognition (CVPR)*, pp. 15979–15988. IEEE, June 2022. doi: 10.1109/cvpr52688.2022.01553. URL <http://dx.doi.org/10.1109/CVPR52688.2022.01553>.

Hoch, T., Schulz, D., Eling, N., Gómez, J. M., Levesque, M. P., and Bodenmiller, B. Multiplexed imaging mass cytometry of the chemokine milieus in melanoma characterizes features of the response to immunotherapy. *Science Immunology*, 7(70), April 2022. ISSN 2470-9468. doi: 10.1126/sciimmunol.abk1692. URL <http://dx.doi.org/10.1126/sciimmunol.abk1692>.

Ilse, M., Tomeczak, J., and Welling, M. Attention-based deep multiple instance learning. In Dy, J. and Krause, A. (eds.), *Proceedings of the 35th International Conference on Machine Learning*, volume 80 of *Proceedings of Machine Learning Research*, pp. 2127–2136. PMLR, 10–15 Jul 2018. URL <https://proceedings.mlr.press/v80/ilse18a.html>.

IMMUcan Consortium. Immucan – an integrated european immuno-oncology profiling platform. <https://immucan.eu/>, 2025. Accessed: 2025-10-26.

Jackson, H. W., Fischer, J. R., Zanotelli, V. R. T., Ali, H. R., Mechera, R., Soysal, S. D., Moch, H., Muenst, S., Varga, Z., Weber, W. P., and Bodenmiller, B. The single-cell pathology landscape of breast cancer. *Nature*, 578(7796):615–620, January 2020. ISSN 1476-4687. doi: 10.1038/s41586-019-1876-x. URL <http://dx.doi.org/10.1038/s41586-019-1876-x>.

Kraus, O., Kenyon-Dean, K., Saberian, S., Fallah, M., McLean, P., Leung, J., Sharma, V., Khan, A., Balakrishnan, J., Celik, S., Beaini, D., Sypetkowski, M., Cheng, C. V., Morse, K., Makes, M., Mabey, B., and Earnshaw, B. Masked autoencoders for microscopy are scalable learners of cellular biology. In *2024 IEEE/CVF Conference on Computer Vision and Pattern Recognition (CVPR)*, pp. 11757–11768. IEEE, June 2024. doi: 10.1109/cvpr52733.2024.01117. URL <http://dx.doi.org/10.1109/CVPR52733.2024.01117>.

Küçükköse, E., Baars, M. J. D., Amini, M., Schraa, S. J., Floor, E., Bol, G. M., Borel Rinkes, I. H. M., Roodhart, J. M. L., Koopman, M., Laoukili, J., Kranenburg, O., and Vercoulen, Y. Stromal localization of inactive cd8+ t cells in metastatic mismatch repair deficient colorectal cancer. *British Journal of Cancer*, 130(2):213–223, December 2023. ISSN 1532-1827. doi: 10.1038/s41416-023-02500-x. URL <http://dx.doi.org/10.1038/s41416-023-02500-x>.

Latonen, L., Koivukoski, S., Khan, U., and Ruusuvuori, P. Virtual staining for histology by deep learning. *Trends in Biotechnology*, 42(9):1177–1191, September 2024. ISSN 0167-7799. doi: 10.1016/j.tibtech.2024.02.009. URL <http://dx.doi.org/10.1016/j.tibtech.2024.02.009>.

Li, C. and Yao, A. KernelWarehouse: Rethinking the design of dynamic convolution. In Salakhutdinov, R., Kolter, Z., Heller, K., Weller, A., Oliver, N., Scarlett, J., and Berkenkamp, F. (eds.), *Proceedings of the 41st International Conference on Machine Learning*, volume 235 of *Proceedings of Machine Learning Research*, pp. 29201–29221. PMLR, 21–27 Jul 2024. URL <https://proceedings.mlr.press/v235/li24cg.html>.

Lo, Y.-C., Keyes, T. J., Jager, A., Sarno, J., Domizi, P., Majeti, R., Sakamoto, K. M., Lacayo, N., Mullighan, C. G., Waters, J., Sahaf, B., Bendall, S. C., and Davis,

K. L. Cytofin enables integrated analysis of public mass cytometry datasets using generalized anchors. *Nature Communications*, 13(1), February 2022. ISSN 2041-1723. doi: 10.1038/s41467-022-28484-5. URL <http://dx.doi.org/10.1038/s41467-022-28484-5>.

Loshchilov, I. and Hutter, F. Decoupled weight decay regularization. In *International Conference on Learning Representations*, 2019. URL <https://openreview.net/forum?id=Bkg6RiCqY7>.

Meyer, L., Jackson, H. W., Eling, N., Zhao, S., Usui, G., Dakhl, H., Schraml, P., Dettwiler, S., Elfgen, C., Varga, Z., Moch, H., de Souza, N., and Bodenmiller, B. A stratification system for breast cancer based on basoluminal tumor cells and spatial tumor architecture. *Cancer Cell*, 43(9):1637–1655.e9, September 2025. ISSN 1535-6108. doi: 10.1016/j.ccr.2025.06.019. URL <http://dx.doi.org/10.1016/j.ccr.2025.06.019>.

Milosevic, V. Different approaches to imaging mass cytometry data analysis. *Bioinformatics Advances*, 3 (1):vbad046, 04 2023. ISSN 2635-0041. doi: 10.1093/bioadv/vbad046. URL <https://doi.org/10.1093/bioadv/vbad046>.

Nat. Methods Editorial. Method of the year 2024: spatial proteomics. *Nature Methods*, 21(12):2195–2196, December 2024. ISSN 1548-7105. doi: 10.1038/s41592-024-02565-3. URL <http://dx.doi.org/10.1038/s41592-024-02565-3>.

Ohara, K., Rendeiro, A. F., Bhinder, B., Eng, K. W., Ravichandran, H., Nguyen, D., Pisapia, D., Vosoughi, A., Fernandez, E., Shohdy, K. S., Manohar, J., Beg, S., Wilkes, D., Robinson, B. D., Khani, F., Bareja, R., Tagawa, S. T., Ouseph, M. M., Sboner, A., Elemento, O., Faltas, B. M., and Mosquera, J. M. The evolution of metastatic upper tract urothelial carcinoma through genomic-transcriptomic and single-cell protein markers analysis. *Nature Communications*, 15 (1), March 2024. ISSN 2041-1723. doi: 10.1038/s41467-024-46320-w. URL <http://dx.doi.org/10.1038/s41467-024-46320-w>.

Quab, M., Darcet, T., Moutakanni, T., Vo, H. V., Szafraniec, M., Khalidov, V., Fernandez, P., HAZIZA, D., Massa, F., El-Nouby, A., Assran, M., Ballas, N., Galuba, W., Howes, R., Huang, P.-Y., Li, S.-W., Misra, I., Rabbat, M., Sharma, V., Synnaeve, G., Xu, H., Jegou, H., Mairal, J., Labatut, P., Joulin, A., and Bojanowski, P. DINoV2: Learning robust visual features without supervision. *Transactions on Machine Learning Research*, 2024. ISSN 2835-8856. URL <https://openreview.net/forum?id=a68SUT6zFt>. Featured Certification.

Papa, L., Russo, P., Amerini, I., and Zhou, L. A survey on efficient vision transformers: Algorithms, techniques, and performance benchmarking. *IEEE Transactions on Pattern Analysis and Machine Intelligence*, 46(12):7682–7700, December 2024. ISSN 1939-3539. doi: 10.1109/tpami.2024.3392941. URL <http://dx.doi.org/10.1109/TPAMI.2024.3392941>.

Rigamonti, A., Viatore, M., Polidori, R., Rahal, D., Erreni, M., Fumagalli, M. R., Zanini, D., Doni, A., Putignano, A. R., Bossi, P., Voulaz, E., Alloisio, M., Rossi, S., Zucali, P. A., Santoro, A., Balzano, V., Nisticò, P., Feuerhake, F., Mantovani, A., Locati, M., and Marchesi, F. Integrating ai-powered digital pathology and imaging mass cytometry identifies key classifiers of tumor cells, stroma, and immune cells in non-small cell lung cancer. *Cancer Research*, 84(7):1165–1177, February 2024. ISSN 1538-7445. doi: 10.1158/0008-5472.can-23-1698. URL <http://dx.doi.org/10.1158/0008-5472.CAN-23-1698>.

Salié, H., Wischer, L., D’Alessio, A., Godbole, I., Suo, Y., Otto-Mora, P., Beck, J., Neumann, O., Stenzinger, A., Schirmacher, P., Fulgenzi, C. A. M., Blaumeiser, A., Boerries, M., Roehlen, N., Schultheiß, M., Hofmann, M., Thimme, R., Pinato, D. J., Longerich, T., and Bengsch, B. Spatial single-cell profiling and neighbourhood analysis reveal the determinants of immune architecture connected to checkpoint inhibitor therapy outcome in hepatocellular carcinoma. *Gut*, 74(3):451–466, September 2024. ISSN 1468-3288. doi: 10.1136/gutjnl-2024-332837. URL <http://dx.doi.org/10.1136/gutjnl-2024-332837>.

Shaban, M., Lassoued, W., Canubas, K., Bailey, S., Liu, Y., Allen, C., Strauss, J., Gulley, J. L., Jiang, S., Mahmood, F., Zaki, G., and Sater, H. A. Deep learning model imputes missing stains in multiplex images. November 2023. doi: 10.1101/2023.11.21.568088. URL <http://dx.doi.org/10.1101/2023.11.21.568088>.

Shaban, M., Chang, Y., Qiu, H., Yeo, Y. Y., Song, A. H., Jaume, G., Wang, Y., Weishaupt, L. L., Ding, T., Vaidya, A., Lamane, A., Shao, D., Zidane, M., Bai, Y., McCallum, P., Luo, S., Wu, W., Wang, Y., Cramer, P., Chan, C. N., Stephan, P., Schaffernath, J., Lee, J. L., Michel, H. A., Tian, C., Almagro-Perez, C., Wagner, S. J., Sahai, S., Lu, M. Y., Chen, R. J., Zhang, A., Gonzales, M. E. M., Makky, A., Lee, J.-Y. J., Cheng, H., Ahmar, N. E., Matar, S., Haist, M., Phillips, D., Tan, Y., Nolan, G. P., Burack, W. R., Estes, J. D., Liu, J. T. C., Choueiri, T. K., Agarwal, N., Barry, M., Rodig, S. J., Le, L. P., Gerber, G., Schürch, C. M., Theis, F. J., Kim, Y. H., Yeong, J., Signoretti, S., Howitt, B. E., Loo, L.-H., Ma, Q., Jiang, S., and Mahmood, F. A

foundation model for spatial proteomics, 2025. URL <https://arxiv.org/abs/2506.03373>.

Sorin, M., Rezanejad, M., Karimi, E., Fiset, B., Desharnais, L., Perus, L. J. M., Milette, S., Yu, M. W., Maritan, S. M., Doré, S., Pichette, E., Enlow, W., Gagné, A., Wei, Y., Orain, M., Manem, V. S. K., Rayes, R., Siegel, P. M., Camilleri-Broët, S., Fiset, P. O., Desmeules, P., Spicer, J. D., Quail, D. F., Joubert, P., and Walsh, L. A. Single-cell spatial landscapes of the lung tumour immune microenvironment. *Nature*, 614(7948): 548–554, February 2023. ISSN 1476-4687. doi: 10.1038/s41586-022-05672-3. URL <http://dx.doi.org/10.1038/s41586-022-05672-3>.

Steenbuck, N., Damond, N., Engler, S., Kusmartseva, I., Posgai, A. L., Drotar, D. M., Williams, M. D., de Souza, N., Brusko, T. M., Brusko, M. A., Wasserfall, C. H., Atkinson, M. A., and Bodenmiller, B. Imaging mass cytometry reveals early β -cell dysfunction and changes in immune signatures during type 1 diabetes progression in human pancreata. *BiorXiv*, March 2025. doi: 10.1101/2025.03.05.641526. URL <http://dx.doi.org/10.1101/2025.03.05.641526>.

Stirn, A., Wessels, H.-H., Schertzer, M. D., Pereira, L. P., Sanjana, N. E., and Knowles, D. A. Faithful heteroscedastic regression with neural networks. In *International Conference on Artificial Intelligence and Statistics*, 2022. URL <https://api.semanticscholar.org/CorpusID:254853633>.

Sussman, J. H., Kim, N., Kemp, S. B., Traum, D., Katsuda, T., Kahn, B. M., Xu, J., Kim, I.-K., Eskandarian, C., Delman, D., Beatty, G. L., Kaestner, K. H., Simpson, A. L., and Stanger, B. Z. Multiplexed imaging mass cytometry analysis characterizes the vascular niche in pancreatic cancer. *Cancer Research*, 84(14): 2364–2376, May 2024. ISSN 1538-7445. doi: 10.1158/0008-5472.can-23-2352. URL <http://dx.doi.org/10.1158/0008-5472.CAN-23-2352>.

Ternes, L., Lin, J.-R., Chen, Y.-A., Gray, J. W., and Chang, Y. H. Computational multiplex panel reduction to maximize information retention in breast cancer tissue microarrays. *PLOS Computational Biology*, 18(9):e1010505, September 2022. ISSN 1553-7358. doi: 10.1371/journal.pcbi.1010505. URL <http://dx.doi.org/10.1371/journal.pcbi.1010505>.

Wenckstern, J., Jain, E., Vasilev, K., Pariset, M., Wicki, A., Gut, G., and Bunne, C. Ai-powered virtual tissues from spatial proteomics for clinical diagnostics and biomedical discovery, 2025. URL <https://arxiv.org/abs/2501.06039>.

Woo, S., Debnath, S., Hu, R., Chen, X., Liu, Z., Kweon, I. S., and Xie, S. Convnext v2: Co-designing and scaling convnets with masked autoencoders. In *2023 IEEE/CVF Conference on Computer Vision and Pattern Recognition (CVPR)*, pp. 16133–16142, 2023. doi: 10.1109/CVPR52729.2023.01548.

Xiao, X., Guo, Q., Cui, C., Lin, Y., Zhang, L., Ding, X., Li, Q., Wang, M., Yang, W., Kong, Y., and Yu, R. Multiplexed imaging mass cytometry reveals distinct tumor-immune microenvironments linked to immunotherapy responses in melanoma. *Communications Medicine*, 2(1), October 2022. ISSN 2730-664X. doi: 10.1038/s43856-022-00197-2. URL <http://dx.doi.org/10.1038/s43856-022-00197-2>.

Zidane, M., Makky, A., Bruhns, M., Rochwarger, A., Babaei, S., Claassen, M., and Schürch, C. M. A review on deep learning applications in highly multiplexed tissue imaging data analysis. *Frontiers in Bioinformatics*, 3, July 2023. ISSN 2673-7647. doi: 10.3389/fbinf.2023.1159381. URL <http://dx.doi.org/10.3389/fbinf.2023.1159381>.

A. Appendix

A.1. Sampling and masking procedures for Masked Modelling task

Each training sample consists of a full measured panel $(\mathbf{X}_{\mathcal{I}_{\text{img}}}, \mathcal{I}_{\text{img}})$ with $\mathbf{X}_{\mathcal{I}_{\text{img}}} \in \mathbb{R}^{C_{\text{img}} \times H \times W}$ where $C_{\text{img}} = |\mathcal{I}_{\text{img}}|$. We construct minibatches using a panel-grouped sampler, so all samples within a minibatch share C_{img} (the same panel size) using the following steps: (i) target-set subsampling, (ii) full-channel dropout within the targets, and (iii) patch-wise spatial masking of the remaining inputs.

(i) Target-set subsampling. For each minibatch we first sample a target size

$$K \sim \text{Unif}\left(\{\lceil \alpha C_{\text{img}} \rceil, \dots, C_{\text{img}}\}\right),$$

where α by default is set to 0.75 and, for each sample, we choose K markers uniformly without replacement from \mathcal{I}_{img} to form \mathcal{I}_{tgt} and the corresponding tensor $\mathbf{X}_{\mathcal{I}_{\text{tgt}}} \in \mathbb{R}^{K \times H \times W}$. Each sample in minibatch has its K markers drawn independently.

(ii) Full-marker dropout within targets. Given K , we drop a non-empty subset of target markers by sampling

$$M \sim \text{Unif}\left(\{1, \dots, \lceil \beta K \rceil\}\right),$$

where β by default is set to 0.5, and selecting $K - M$ markers uniformly without replacement from \mathcal{I}_{img} to form the encoder input set $\mathcal{I}_{\text{in}} \subset \mathcal{I}_{\text{tgt}}$. The dropped channels $\mathcal{I}_{\text{tgt}} \setminus \mathcal{I}_{\text{in}}$ are completely unobserved by the encoder, but are included in the reconstruction targets. Each sample in minibatch has its $K - M$ channels drawn independently. This setting simulates a virtual staining scenario, where models aims at prediction of the markers missing from panel.

(iii) Patch-wise spatial masking. On the remaining input channels \mathcal{I}_{in} , we follow a masking protocol from (Woo et al., 2023) and additionally mask spatial patches by setting them to zero. Let $p = 8$ and assume p divides H and W . Define $(h, w) = (H/p, W/p)$ and sample a Bernoulli mask on the patch grid

$$\mathbf{m} \in \{0, 1\}^{|\mathcal{I}_{\text{in}}| \times h \times w}, \quad \mathbb{P}[\mathbf{m}_{c,u,v} = 1] = \rho,$$

where ρ by default is set to 0.6. We then expand each entry of \mathbf{m} to a $p \times p$ block to obtain $\mathbf{M} \in \{0, 1\}^{|\mathcal{I}_{\text{in}}| \times H \times W}$ and define the masked encoder input

$$\tilde{\mathbf{X}}_{\mathcal{I}_{\text{in}}} = \mathbf{X}_{\mathcal{I}_{\text{in}}} \odot (1 - \mathbf{M}),$$

where \odot denotes elementwise multiplication.

A.2. Stabilizing log-variance training using a gradient clamping

To avoid numerical issues when $\hat{\ell} = \exp\left(\mathbf{X}_{\mathcal{I}_{\text{tgt}}}^{\log \sigma^2}\right)$ becomes extremely small or large, we apply a clamped log-variance

$$\hat{\ell} = \text{clamp}(\ell; a, b), \quad (a, b) = (-15, 15).$$

In the *forward pass*, clamp returns the hard clip $\text{clip}(\hat{\ell}; a, b) = \min(\max(\hat{\ell}, a), b)$. In the *backward pass*, the gradient is propagated unchanged inside the interval and is smoothly downweighted outside it:

$$\frac{\partial \text{clamp}(\ell; a, b)}{\partial \ell} = \begin{cases} 1, & a < \ell < b, \\ 1 - \tanh^2(\ell), & \ell \leq a \text{ or } \ell \geq b. \end{cases}$$

A.3. Dataset details

IMC17M is a curated aggregation of 28 IMC datasets comprising 25 distinct marker panels, totalling 24,405 images and 265 unique markers across 14 histologies. A detailed composition of used datasets is presented in [Table 4](#). Throughout, we use *dataset* to denote a source study/cohort, and *panel* to denote its measured marker configuration; multiple datasets may share a panel, and a single study may provide multiple panels (e.g., protocol variants).

The corpus spans diverse biological contexts, including tumour microenvironments (e.g., breast, lung, glioblastoma, colorectal, melanoma, oral squamous cell carcinoma, urothelial carcinoma), immune system characterisation, and tissue-specific studies (e.g., pancreas in Type I diabetes and organoids). Panel sizes range from 28 to 47 markers, with most panels in the 35–45 range, reflecting the strong marker-set heterogeneity typical of IMC collections.

For all experiments, we partition images into train/test with a 4:1 ratio, stratified by panel to ensure that each panel contributes proportionally to both splits and to reduce confounding by panel-specific acquisition characteristics. Table 4 reports per-dataset counts and histopathologies; datasets labelled IMMUcan are consortium data and are currently proprietary (awaiting publication).

Table 4. Overview of the IMC dataset used for model training and evaluation. IMMUcan BC2 and IMMUcan SCCHN1 datasets are IMMUcan (IMMUcan Consortium, 2025) proprietary data, awaiting publication.

Dataset	Images	Markers	Histopathology
ajaib (Ajaib et al., 2025)	34	34	Glioblastoma
bengsch (Salié et al., 2024)	108	42	Hepatocellular carcinoma
bowen-lynch (Bowen et al., 2023)	85	38	Lynch Syndrome colorectal mucosa
cho (Cho et al., 2025)	140	41	Pancreatic adenocarcinoma
cords (Cords et al., 2024)	2070	42	Non-small cell lung cancer
cords-fibro (Cords et al., 2023)	110	42	Breast cancer
damond (Damond et al., 2019)	845	36	Type I diabetes pancreas
danenbergs (Danenbergs et al., 2022)	794	39	Breast cancer
ehret-p1 (Ehret, 2025)	56	42	Organoid
ehret-p2 (Ehret, 2025)	52	44	Organoid
einhaus (Einhäusler et al., 2023)	94	41	Oral squamous cell carcinoma
haley-glio (Haley et al., 2024)	24	40	Glioblastoma
hoch-protein (Hoch et al., 2022)	167	46	Melanoma
hoch-rna (Hoch et al., 2022)	166	41	Melanoma
IMMUcan BC2 (IMMUcan Consortium, 2025)	813	40	Breast cancer
IMMUcan NSCLC2 (P1) (Eling et al., 2025)	745	40	Non-small-cell lung cancer
IMMUcan NSCLC2 (P2) (Eling et al., 2025)	566	44	Non-small-cell lung cancer
IMMUcan SCCHN1* (IMMUcan Consortium, 2025)	743	40	Head and neck cancer
jackson-basel (Jackson et al., 2020)	381	39	Breast cancer
jackson-zurich (Jackson et al., 2020)	365	39	Breast cancer
kucukkose (Küçükköse et al., 2023)	27	34	Colorectal cancer
meyer (Meyer et al., 2025)	495	39	Breast cancer
ohara (Ohara et al., 2024)	58	28	Urothelial carcinoma
rigamonti (Rigamonti et al., 2024)	158	29	Non-small-cell lung cancer
steenbuck-immune (Steenbuck et al., 2025)	7557	47	Type I diabetes pancreas
steenbuck-islets (Steenbuck et al., 2025)	7558	47	Type I diabetes pancreas
sussman (Sussman et al., 2024)	35	35	Pancreatic adenocarcinoma
xu (Xiao et al., 2022)	158	37	Melanoma

* IMMUcan SCCHN1 was held out from training for all models (ImmuviS, ImmuviS_{ViT}, and VirTues) and used for zero-shot evaluation.

A.4. IMC Preprocessing Pipeline

IMC raw image data requires additional preprocessing prior to model training. We apply the following steps in order.

Arcsinh transformation. We apply a pixel-wise arcsinh transform with cofactor 5 to compress the high dynamic range of IMC intensities while amplifying foreground signal and accommodating zero/negative values.

Denoising via low-pass filtering. We observed that IMC-specific background noise and hot pixels that can destabilize optimization, particularly when training on smaller image crops. To this issue we applied a Butterworth filter (Butterworth, 1930) that attenuates high-frequency spatial noise while maintaining a maximally flat passband response.

Panel-wise intensity standardization. We further normalize marker intensities to a [0, 1] interval using a modified min–max scaling applied independently per dataset panel. We fix the lower bound at 0 and set the upper bound to the 99th

percentile of the pooled intensity distribution across all markers within the panel, rounded up to one decimal place. This improves cross-dataset comparability while limiting the influence of extreme outliers.

Subimage extraction and augmentation. The model input is a 128×128 crops, where each pixel corresponds to approximately $1 \mu\text{m}^2$ tissue area. To mitigate I/O bound during training, we extracted non-overlapping subimages of shape 256×256 from the training split images. During training, we apply random rotation, reflection and cropping to generate crops from subimages of intended shape. For one training epoch, all subimages from all images are used once. During evaluation, we extract image crops via a deterministic central crop from each source image to ensure consistency and reproducibility.

A.5. ImmuVis Models configurations

In this section we introduce the detailed architecture of ImmuVis and ImmuVis_{ViT} subnetworks. The details of all architectures configurations are shown in [Table 5](#).

Table 5. ImmuVis model architecture and parameter specifications

Component	Parameter	Value / Specification
ImmuVis		
Encoder (Marker-Agnostic)	Stages (L_{ma})	1
	Stage composition	4-fold Downsampling + 6 ConvNeXt v2 blocks
	Stage dimension (d_{ma})	16
Encoder (Pan-Marker)	Hyperkernel size ($h_e \times w_e$)	1×1
	Pan-Marker dimension (d_{pm})	192
	Stages (L_{pm})	2
	Stage composition	4-fold Downsampling + 6 ConvNeXt v2 blocks
	Stage dimensionalities	384, 768
Latent feature map	Dimension (d_{lat})	768
	Shape ($H_{lat} \times W_{lat}$)	16×16
Decoder	Hyperkernel size ($h_d \times w_d$)	1×1
	Marker-Specific dimension (d_{ms})	512
	Marker-Agnostic decoder	1 ConvNeXt v2 Block ($B_{dec} = 1$)
ImmuVis_{ViT}		
Encoder (Marker-Agnostic)	Stages (L_{ma})	0 (Identity)
	Dimension (d_{ma})	1
Encoder (Pan-Marker)	Hyperkernel / Patch size ($h_e \times w_e$)	8×8 (Stride 8)
	Pan-Marker dimension (d_{pm})	768
	Layers	12
	Attention heads	12
Latent feature map	Dimension (d_{lat})	768
	Shape ($H_{lat} \times W_{lat}$)	16×16
Decoder	Hyperkernel size ($h_d \times w_d$)	1×1
	Marker-Specific dimension (d_{ms})	768
	Marker-Agnostic decoder	1 ViT Block ($B_{dec} = 1$)

A.5.1. MARKER-CONDITIONAL KERNEL GENERATORS

For both encoder and decoder generators ϕ_e, ϕ_d we first map markers to their vocabulary indices $i \in \mathcal{N}$. Then, each marker index is assigned to a standard learnable embedding of a flattened intended kernel shape (either $d_{pm} \cdot d_{ma} \cdot h_e \cdot w_e$ for encoder and $d_{ms} \cdot d_{lat} \cdot h_d \cdot w_d$ for decoder), subsequently reshaped to the final kernel dimensions.

A.5.2. MARKER-AGNOSTIC DECODER ARCHITECTURE

Let \mathbf{U}_{j^c} be the output of the decoder Hyperconvolution operator \mathfrak{H}_d for target marker j^c . Then \mathfrak{R} of the marker-agnostic decoder Dec_{ma} performs the following steps:

$$\begin{aligned}\mathbf{D}_{j^c} &= \text{Blocks}^{(B_{\text{dec}})}(\mathbf{U}_{j^c}) \\ \mathbf{P}_{j^c} &= \text{Conv}_{1 \times 1}(\mathbf{D}_{j^c}, 2\lambda^2) \\ \hat{\mathbf{X}}_{j^c} &= \text{PixelShuffle}(\mathbf{P}_{j^c})\end{aligned}$$

where $\lambda = 8$ is the total upsampling factor. Since in the preprocessing stage of IMC17M we normalize marker intensities to a $[0, 1]$ interval, we map

$$\hat{\mathbf{X}}^0 = \text{sigmoid}(\hat{\mathbf{X}}^0).$$

A.5.3. COMMENT ON THE $\text{IMMUVIS}_{\text{ViT}}$ ARCHITECTURE

For $\text{ImmuVis}_{\text{ViT}}$ we initially evaluated a configuration analogous to ImmuVis that employed a one-stage Marker-agnostic encoder, however training of this configuration diverged. Subsequently, we investigated a pixel-wise hyperkernel embedding strategy equivalent to the $L_{\text{ma}} = 0$ configuration, followed by a standard patch tokenizer, but it also suffered from the convergence difficulties. Consequently, we adopted the minimal strategy with the hyperkernel acting directly as a multiplex tokenizer (Enc_{ma} was set as an identity), creating pan-marker patch embeddings from the original input.

A.6. Optimization and training protocol.

All models are trained with AdamW (Loshchilov & Hutter, 2019) using weight decay 10^{-4} and a cosine annealing learning-rate schedule with linear warmup. The learning rate increases linearly during the first 5 epochs to a peak of 5×10^{-4} , and is then annealed to a final value of 10^{-6} by the end of training. We use mixed-precision training with `bfloat16` for efficiency. We used batch size of 8, as we observed lower batches tend to improve the convergence of models. We additionally apply ℓ_2 -norm gradient clipping with maximum norm 1.0. We train all ImmuVis variants for 200 epochs.

A.7. Single-cell pre-processing

For each segmented cell from the (Eling et al., 2025) dataset, we extract a 32×32 pixel patch centred at the cell mask centroid. All pixels outside the target cell mask are zeroed to remove neighborhood information while preserving within-cell marker intensities. Each crop is encoded by the frozen encoder (no fine-tuning) of all considered models ImmuVis , $\text{ImmuVis}_{\text{ViT}}$, and VirTues to obtain a spatial embedding map, which we reduce to a fixed-length vector (d_{lat}) via spatial average pooling.